Journal of Materials Chemistry A

ROYAL SOCIETY OF CHEMISTRY

PAPER

View Article Online
View Journal | View Issue

Cite this: J. Mater. Chem. A, 2023, 11, 12308

Harnessing solar energy for electrocatalytic biorefinery using lignin-derived photothermal materials†

Xinpeng Zhao,‡[a] Lei Shi,‡[b] Bing Tian,[a] Shujun Li,[a] Shouxin Liu,[a] Jian Li,[a] Song Liu,*[b] Tony D. James *[cd] and Zhijun Chen *[a]

Received 18th February 2023
Accepted 10th May 2023

DOI: 10.1039/d3ta01023f

rsc.li/materials-a

The bio-refinery of lignocellulose exhibits great potential for sustainable development. However, technical barriers for proper utilization of lignin and heavy energy consumption have challenged the profitability and sustainability of such biorefineries. Here, we efficiently converted lignin to photothermal materials (D-Lig-Fe) by the demethylation of lignin and coordinating with Fe^{3+}, producing electricity that could be utilized for the electrocatalytic conversion of 5-hydromethyl-2-furaldehyde (HMF) to 2,5-furandicarboxylic acid (FDCA) when coupled with a thermoelectric generator (TEG) in the bio-refinery. Specifically, D-Lig-Fe exhibited robust and high photothermal efficiency (~36%), producing electricity up to 1.6 V upon natural solar irradiation assisted by a Fresnel lens together with TEG. The as-generated electricity drove a high-yielding conversion of HMF to FDCA *via* NiCoB catalyst-based electrocatalysis in the bio-refinery. We anticipate that this research will help establish an efficient and practical approach toward an integrated biorefinery.

Introduction

A bio-refinery is responsible for converting biomass resources into chemicals and functional materials.[1,2] The development of bio-refineries has become a hot topic worldwide, since the reduction of CO_2 emission and the safeguarding of the environment are essential goals.[3]

Amongst all available biomass, lignocellulosic resources, consisting of cellulose, hemicellulose and lignin, are the most abundant and are promising materials for use in the bio-refinery.[4–6] There are multiple steps involved in the lignocellulosic bio-refinery including fractionation of cellulose, hemicellulose and lignin, conversion of those components to platform compounds and preparation of targeted chemicals/materials from these platform compounds.[7–11] To achieve an improved efficiency of the lignocellulosic bio-refinery, effective deep eutectic solvents, a "lignin first" strategy and stabilization strategies have been proposed for improving the pre-treatment/depolymerization of biomass resources.[12–16] Thermocatalytic, photocatalytic and electrocatalytic methods have been developed for converting biomass-derived platform compounds to valuable materials or chemicals.[17–24] Amongst them, the HMF-to-FDCA conversion using electrocatalytic methods has received particular attention.[25] That is because FDCA is a perfect replacement for terephthalic acid which is used to prepare one of the most common thermoplastics.[26] Additionally, the electrochemical pathway operates using low cost electrocatalysts and under mild conditions (*i.e.* ambient temperature and pressure), yet it achieves high activity and selectivity for converting HMF to FDCA.[20,21,27] Notably, heavy electricity consumption increases the cost of the electrocatalytic process.

Although several value-added chemicals and materials have been obtained from the lignocellulosic bio-refinery,[28–31] technical barriers for the proper utilization of lignin have challenged the profitability and sustainability of biorefineries, which has been attributed to the complex and heterogeneous structure of lignin.[32,33]

With our previous research we exploited the potential for the photothermal conversion of lignin albeit with a low efficiency (~20%).[34,35] Additionally, utilizing the abundant and renewable solar energy to generate thermal energy *via* photothermal conversion results in full-spectrum utilization with high efficiency.[36–39] Motivated by this, we integrated the photothermal conversion of lignin derivatives with a NiCoB catalyst-based electrocatalytic method to construct a solar–thermal–electrocatalytic process for use in biorefineries (Fig. 1).

[a]Key Laboratory of Bio-based Material Science & Technology, Northeast Forestry University, Ministry of Education, Harbin 150040, China. E-mail: chenzhijun@nefu.edu.cn

[b]College of Chemistry, Chemical Engineering and Resource Utilization, Northeast Forestry University, Harbin 150040, China. E-mail: carlosliusong@nefu.edu.cn

[c]Department of Chemistry, University of Bath, Bath BA2 7AY, UK. E-mail: T.D.James@bath.ac.uk

[d]School of Chemistry and Chemical Engineering, Henan Normal University, Xinxiang 453007, PR China

† Electronic supplementary information (ESI) available. See DOI: https://doi.org/10.1039/d3ta01023f

‡ These authors contributed equally to this work.

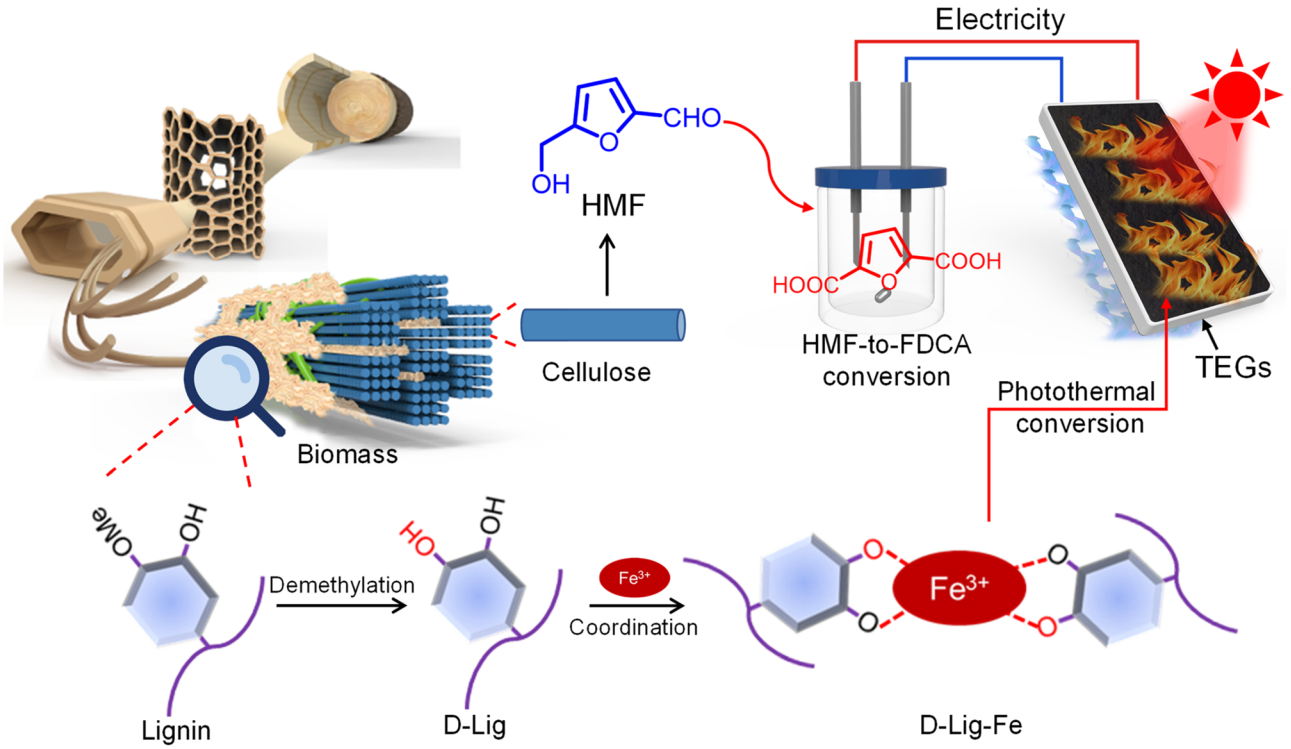

Fig. 1 Schematic illustration for the preparation of lignin-derived photothermal materials and the solar–thermal–electrocatalytic process for the integrated biorefinery.

Specifically, we removed the methyl moieties from lignin. Then the as-obtained D-Lig was coordinated with Fe^{3+} to generate D-Lig-Fe which exhibited efficient photothermal conversion. The photothermal conversion was used to generate electricity in combination with a thermoelectric generator (TEG). As such, 5-hydroxymethylfurfural (HMF) was oxidized to 2,5-furandicarboxylic acid (FDCA) selectively and in a high yield in the presence of the NiCoB catalysts and driven by the as-generated electricity from the photothermal process.

Results and discussion

Characterization of D-Lig-Fe

D-Lig was obtained by removing the methyl moieties of lignin assisted by BF_3. 2D HSQC NMR spectra indicated that the intensity of signals assigned to the methyl moieties of D-Lig (δ_C/δ_H 50–75/2.5–4.5) significantly decrease (Fig. 2a), when compared with raw lignin. Additionally, FC titration proved that the amount of phenolic moieties increased from 91 μmol g^{-1} to 129 μmol g^{-1} (Fig. S1†).[40] D-Lig was then mixed with Fe^{3+} to generate D-Lig-Fe in aqueous solution. Elemental mapping indicated that iron was evenly distributed in the D-Lig matrix (Fig. 2b). Comparison of the electron spin resonance (ESR) spectrum between D-Lig and D-Lig-Fe indicated that D-Lig-Fe exhibited a significant decrease in the intensity of the radical spin signal (*g*-factor = 2.0049) (Fig. S2†). This signal originates from the semiquinone structure or quinone structure, which are isomeric forms of the free phenolics. Thus, the result suggested that the phenolics in D-Lig were coordinated with ferric

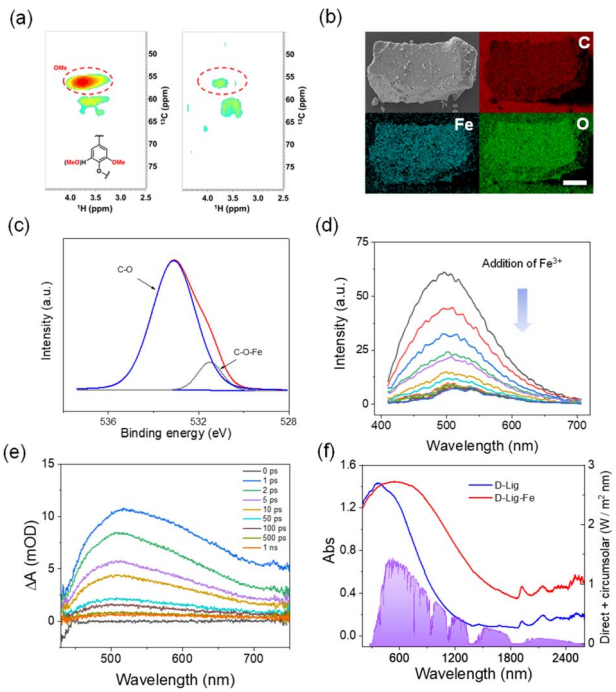

Fig. 2 The characterization of D-Lig-Fe. (a) 2D HSQC NMR of lignin (left) and D-Lig (right). (b) Elemental mapping of D-Lig-Fe (scale bar = 100 μm). (c) O 1s spectra of D-Lig-Fe. (d) Fluorescence spectra of D-Lig-Fe upon addition of Fe^{3+}. (e) fs-TAS spectra of D-Lig-Fe. (f) UV-vis-NIR absorbance of D-Lig and D-Lig-Fe.

ion (Fe^{3+}).[41,42] Raman spectral signals (530–730 cm^{-1}) originating from the coordination of Fe^{3+} and oxygen atoms of the catechol were consistent with the ESR analysis (Fig. S3†).[43,44] Additionally, a C–O–Fe bond (at 531.5 eV) was observed in the high-resolution O 1s, further confirming coordination between D-Lig and Fe^{3+} (Fig. 2c).[45] Additional investigation indicated that coordination between D-Lig and Fe^{3+} decreased the fluorescence emission of D-Lig (Fig. 2d). Generally, fluorescence and photothermal activity are caused by competitive radiative and non-radiative migration of excitons. Decreased fluorescence suggests enhanced non-radiative migration, which is beneficial for photothermal conversion. To gain deeper insight into the activated non-radiative decay processes of D-Lig-Fe, femtosecond transient absorption (fs-TA) spectroscopic analysis (pumped at 365 nm and probed between 400 and 800 nm) was performed. Upon photoexcitation, a broad excited-state absorption (ESA) from 430 to 700 nm was observed for D-Lig-Fe (Fig. 2e). A rapid decay of the ESA band was observed just after 1 ps. The excited state begins to decay from 1 ps to 1 ns. Upon fitting the dynamics, three-time constants of 1.386 ps (τ_1), 47.42 ps (τ_2) and 125.0 ps (τ_3) were obtained at 520 nm, which could be assigned to the internal conversions (Fig. S4†).[46–48] Non-radiative decay mainly took place through internal conversion. Moreover, UV-vis-NIR spectra indicated that D-Lig-Fe exhibited red-shifted absorbance in the visible and NIR region, compared to the D-Lig (Fig. 2f). Such red-shifted absorbance of D-Lig-Fe was attributed to ligand-to-metal electron transfer from D-Lig to Fe^{3+}. The red-shifted absorbance matched the solar spectra, indicating that D-Lig-Fe can efficiently utilize the visible and NIR photons from the solar spectra for thermal heat generation. All these results confirmed that D-Lig-Fe obtained by coordination between D-Lig and Fe^{3+} exhibits great potential for photothermal heat conversion.

Photothermal conversion of D-Lig-Fe

Encouraged by the promoted non-radiative channel and broad absorbance, D-Lig-Fe was evaluated for photothermal conversion. D-Lig-Fe exhibited a temperature increase from 33 °C to 78 °C upon mimetic solar irradiation (100 mW cm^{-2}) with a photothermal efficiency of 36% (Fig. 3a and b). Notably, the photothermal efficiency was higher than that for the reported lignin nanoparticles and even carbon nanotubes under the same conditions (Fig. S5†).[35,49] Further increasing the intensity of mimetic solar sources from 100 mW cm^{-2} to 500 mW cm^{-2}, the temperature increased from 78 °C to 200 °C (Fig. 3a and b). Additionally, D-Lig-Fe was exposed to the mimetic solar irradiation (100 mW cm^{-2}) for 8 "on–off" cycles, and exhibited reversible temperature changes, suggesting good controllability (Fig. S6†). Moreover, D-Lig-Fe exhibited stable photothermal conversion and maintained a stable efficiency of 36% either after UV aging for 12 h, in a humid environment (90%) for 12 h (RH) or storage for 1 month (Fig. 3c). Thermogravimetric curves indicated that D-Lig-Fe lost 4.4% of water weight from 0 to 100 °C. After that, 5.2% weight loss was observed which was due to slight pyrolysis and carbonization.[50] The temperature change curves also indicated a ~46 °C temperature increase of the

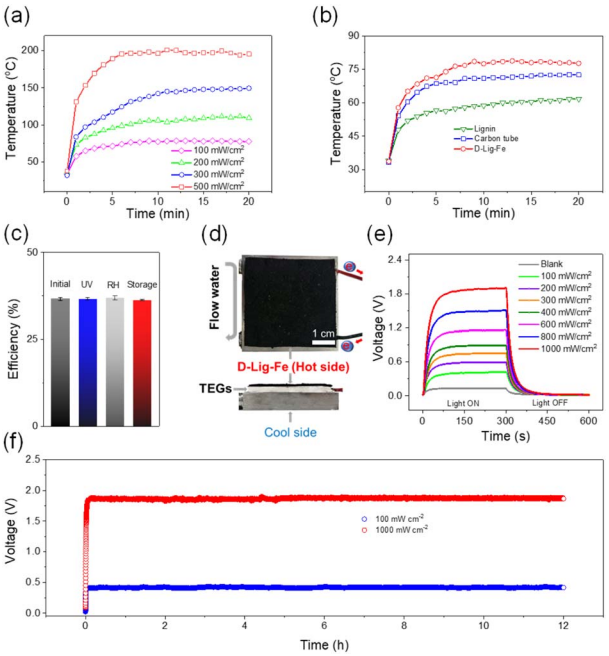

Fig. 3 Photothermal conversion of D-Lig-Fe. (a) Time-dependent temperature change of lignin, carbon tubes and D-Lig-Fe upon 1 sun mimetic solar irradiation. (b) Time-dependent temperature change of D-Lig-Fe upon mimetic solar irradiation at different intensities. (c) Efficiency of photothermal conversion of D-Lig-Fe upon mimetic solar irradiation. (d) Images of the setup for solar–thermal–electricity conversion. (e) Voltage output of the setup (d) upon solar irradiation at different intensities and after switching the irradiation sources off. (f) Voltage output of the setup (d) upon solar irradiation for 12 h.

samples after treatment at 80 °C, 100 °C, and 150 °C for 1 h, which is similar to the non-thermal treated samples. All these results confirmed the good thermal stability of D-Lig-Fe (Fig. S7 and S8†). Encouraged by these results, we subsequently investigated using D-Lig-Fe to drive a TEG. D-Lig-Fe, a thermoelectric module and a cooling system were combined to create a solar-powered TEG assisted by heat-conducting silicone grease (Fig. 3d). The D-Lig-Fe absorbed solar light and heated the thermoelectric module on one side, creating a temperature difference from the other side nearest to the cooling system, and generated a voltage of ~0.41 V (Fig. 3e). A control experiment, in which the TEG without decoration with D-Lig-Fe was used, produced only ~0.13 V voltage upon solar irradiation, confirming that the voltage was indeed triggered and enhanced by solar-to-thermal energy conversion provided by the D-Lig-Fe. The voltage produced by the device increased from 0.41 V to 1.90 V on increasing the intensity of the light from 100 mW cm^{-2} to 1000 mW cm^{-2} (Fig. 3e). Notably, the as-prepared TEG was sensitive to photo irradiation. Switching off the light source immediately reduced the voltage generated by the TEG, demonstrating the good controllability of the device. Upon cycling solar irradiation on and off 6 times (Fig. S9†), the voltage produced was not obviously changed indicating that the system exhibits outstanding photostability. Moreover, the voltage output did not show any obvious change after exposure of the as-built setup to mimetic solar sources for 12 h (Fig. 3f), further

confirming the long-term durability. The as-generated electricity could also be used to power the motion of an engine and turn on a light bulb (Videos S1 and S2†).

Electrochemical conversion of HMF into FDCA

NiCoB supported on nickel foam was prepared as an electrochemical catalyst. We chose this catalyst because of two factors. (a) NiCo transition metals are abundant and cheap, compared to expensive metal-based catalysts used for HMF conversion. (b) NiCo alloys exhibit good adsorption for HMF, enhancing the catalytic performance for HMF conversion.[51]

SEM and TEM confirm that the as-synthesized catalysts are cohesive nanoparticles with an average size of 40 nm (Fig. 4a). Electron diffraction and XRD spectra reveal the amorphous state of the as-prepared catalysts (Fig. 4b and S10†). The HMFOR activity of the NiCoB catalyst was evaluated in an H-type electrolytic cell using linear sweep voltammetry (LSV). The onset potential of NiCoB measured in the electrolyte with 5 mM HMF (1.6 V) was lower than that measured in the electrolyte without HMF (1.7 V), suggesting outstanding electrocatalytic HMFOR activity on the NiCoB electrode (Fig. 4c). Furthermore, the Tafel slope of the OER and HMFOR on the NiCoB was calculated to be 58.7 mV dec^{-1} and 30.3 mV dec^{-1}, respectively, indicating a faster electron-transfer rate (Fig. S11†). The R_{ct} of HMFOR (Ω) was smaller than that of the OER (Ω) in electrochemical impedance spectroscopy (EIS), demonstrating that the progress of HMFOR has faster charge transfer rate (Fig. S12†). Encouraged by these results, solar–thermal–electrochemical catalytic conversion was conducted. First of all, the conversion of HMF was evaluated at different photothermal-induced voltage outputs (1.5 V, 1.6 V, 1.7 V) (Fig. S13†). The most efficient HMF conversion (>99%) and the highest FDCA yield (>80%) were obtained at a voltage of 1.6 V. At lower potentials, the conversion yield was low (~49%), since HMF was easily decomposed to humin under the reaction conditions.[52] At a higher potential (1.7 V), the conversion efficiency was ~78%, which was also lower than the value at 1.6 V. This is because of a competing reaction involving the oxygen evolution reaction (OER). Significantly, our research exhibited competitive performance, when compared with other electrocatalysts for HMF-to-FDCA conversion driven by conventional sources of electricity (Fig. S14†). The HMF-to-FDCA conversion was determined by high-performance liquid chromatography (HPLC) analysis (Fig. S15 and Table S1†). Interestingly, the HMF-to-FDCA oxidation did not exhibit any obvious change after four cycles (Fig. 4d). Encouraged by this result, we conducted an outdoor experiment using natural solar light assisted by a Fresnel lens (Fig. 4e). The real solar intensity was recorded and ranged from 33 mW cm^{-2} to 87 mW cm^{-2} (Fig. S16†). The photothermal efficiency of D-Lig-Fe did not change after solar irradiation using a Fresnel lens, suggesting good photothermal stability (Fig. S17†). Our as-built setup produced a stable output of more than ~1.6 V voltage and ~25 mA cm^{-2} current density upon natural solar irradiation. 75% HMF-to-FDCA conversion was achieved after 4 h in an authentic field experiment (Fig. 4f). Notably, affected by the instability of the real solar light in the outdoor environment (Fig. S16†), the catalytic performance was compromised, and the yield decreased slightly, compared to the lab-based results. Specifically, when the solar intensity is low, lower than 60 mW cm^{-2}, the voltage generated did not reach 1.6 V, which could not then trigger the reaction. As a result, the conversion was stopped during this period, which resulted in a lower overall conversion yield.

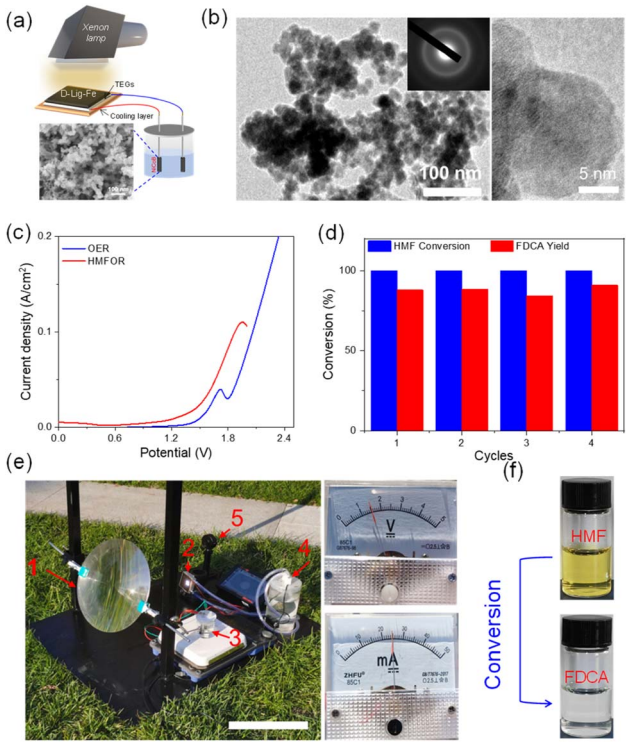

Fig. 4 Solar–thermal–electrocatalytic process. (a) Schematic illustration of electrochemical conversion of HMF into FDCA assisted by the solar–thermal–electric conversion process. Inset: SEM images of NiCoB supported on nickel foam; (b) TEM image (left), HRTEM image (right) and SAED pattern (inset) of NiCoB supported on nickel foam; (c) LSV curves of NiCoB; (d) HMF-to-FDCA conversion yield; (e) images of the setup for an authentic field experiment. (1) Fresnel lens; (2) TEGs; (3) quartz reactor; (4) cooling system; (5) solar meter. Scale bar = 20 cm; (f) images of HMF-to-FDCA conversion.

Conclusions

D-Lig-Fe was prepared using demethylated lignin-iron coordination with a photothermal efficiency of 36%. The photothermal conversion of D-Lig-Fe was stable and did not decrease after UV aging, high humidity treatment and long-term storage. Using these significant advantages, solar–thermal–electricity conversion was achieved using the D-Lig-Fe together with TEGs. The as-generated voltage was then used for the electrocatalytic conversion of HMF to FDCA in a high conversion yield. Moreover, the conversion was successfully achieved under authentic field conditions. Using this strategy, we anticipate that more lignocellulosic source-derived platform compounds can be converted to chemicals using appropriate and efficient electrocatalysts. Thus, our method was general and could further encourage practical applications in the integrated biorefinery.

Experimental

Materials and methods

Lignin was prepared as previously described.[53] Boron tribromide, iron chloride, sodium hydroxide, and dichloromethane were purchased from Aladdin (Shanghai, China) and used as received without further purification. Deionized water was produced using a smart-RO ultrapure water system (Hitech Instruments Co., Ltd, Shanghai, China). TEGs, voltage regulation and other components of the solar–thermal–electricity process were purchased from Taobao (Alibaba, Hangzhou, China). 5-Hydroxymethylfurfural (HMF, 99%), 2,5-furandicarboxylic acid (FDCA, 98%), 2-formyl-5-furancarboxylic acid (FFCA, 98%), 2,5-diformylfuran (DFF, 98%), 5-hydroxymethyl-2-furancarboxylic acid (HMFCA, 98%), potassium hydroxide (KOH), nickel(II) acetate tetrahydrate (98%), cobalt(II) acetate (99%), potassium hydroxide (granular 99.99% trace metals basis), methanol, and ammonium formate were obtained from Sigma-Aldrich. Nickel foam (NF, thickness 0.5 mm) was purchased from Suzhou Shuertai Industrial Technology Co., Ltd, China. Methanol was of chromatographic grade, and the other chemicals were of analytical grade.

Characterization

UV-vis-NIR absorption spectra were recorded using a UV-3600 plus spectrophotometer (SHIMADZU Co., Ltd, China). 2D HSQC NMR spectra were recorded on a Bruker 700 MHz NMR spectrometer with TMS as the internal standard. Photoluminescence (PL) measurements were performed using an FLS1000 fluorescence spectrophotometer (Edinburgh Instruments, Inc., Livingston, U.K.) equipped with a 150 W xenon lamp as the excitation source. X-ray photoelectron spectroscopy was conducted using Kα (Thermo Scientific U.S.). Solar irradiation was recorded with a CEL-NP2000-2A automatic optical power meter (Beijing China Education Au-light Technology Co., Ltd, China). Solar irradiation was simulated using a PLS-SXE300 xenon lamp light source (Perfect Light Co., Ltd, Beijing, China). Thermogravimetric analysis was performed on a Q600 (TA Instruments U.S.). Fourier-transform infrared spectra were recorded on a Nicolet IS 5 FTIR (Thermo Scientific U.S.). Electron spin resonance (ESR) spectra were measured on a Bruker ELEXSYS E500 spectrometer. The crystallinity and phases of the samples were characterized by X-ray diffraction with Cu Kα radiation (λ = 1.5418 Å, XRD-6100, Shimadzu, Japan). The particle size, composition, and morphology were studied by scanning electron microscopy (SEM, JSM-7500F, Japan) and transmission electron microscopy (TEM, JEM-2100, Japan) equipped with SAED. fs-TA spectra were collected on a Helios (Ultrafast Systems U.S.).

Preparation of D-Lig

To a solution of lignin (1 g) in anhydrous CH_2Cl_2 (100 mL), boron tribromide (in dichloromethane, 1 M, 20 mL) was added at 0 °C dropwise slowly. Then, the reaction was maintained at room temperature for 24 h and quenched with cold water slowly. The as-precipitated D-Lig powder was washed with deionized water three times.

Preparation of D-Lig-Fe

The pH of D-Lig aqueous solution (1 g, 20 mL water) was adjusted to 12. After that, ferric chloride solution (10 mL, 0.5 M) was added to the D-Lig solution (20 mL, 1 g). The mixture was then stirred for 3 h at room temperature. The precipitated powder obtained by centrifugation was washed with water twice. The as-obtained powders were dried at 60 °C to give D-Lig-Fe.

Preparation of the amorphous NiCoB catalyst

Nickel foam (NF) was cut into small pieces with dimensions of 1.0 × 2.0 cm^2. These small pieces were ultrasonicated for 1 h with an aqueous solution (0.1 M HCl), ethanol, and ultrapure water, respectively. For the preparation of the amorphous nickel–cobalt alloy catalyst, 1 mmol of $Ni(CH_3COO)_2 \cdot 4H_2O$ and $Co(CH_3COO)_2$ with the molar ratios of Ni to Co(1 : 1) were added to 20 mL of deionized (DI) water in a beaker under magnetic stirring for 10 min, 4 mL of 1.28 M $NaBH_4$ aqueous solution was prepared in another small beaker. Alternate dropping of the two solutions onto clean nickel foam was performed until the nickel foam was completely blackened.

Calculation of photothermal conversion efficiency

Photothermal conversion efficiency was determined in an aqueous solution of D-Lig-Fe and carbon nanotubes (1 mg mL^{-1}, 1 mL) in a vessel with an insulating layer and by illuminating the aqueous solution with artificial solar light (100 mW cm^{-2}). The temperature of the solution was recorded using a digital thermometer, and the photothermal conversion efficiency (η) was estimated from eqn (1):[54]

$$\eta = \frac{Q}{E} = \frac{Cm\Delta T}{PSt} = \frac{C\rho V\Delta T}{PSt} \quad (1)$$

where Q is the thermal energy generated and E is the total energy of incident light. Q is determined by the heat capacity (C), density (ρ), volume (V), and ΔT over 5 min irradiation of the solution. E is determined by the power of the incident light (P), irradiation area (S), and irradiation time (t). The values of C (4.2 J g^{-1} per °C), S (3.14 cm^2), and ρ (1 g cm^{-3}) for water were used in calculations.

Electrochemical measurements

We conducted electrochemical measurements on a CHI 760E electrochemical workstation. Electrochemical data were collected at room temperature in a common electrolytic cell (100 mL). The electrochemical tests were carried out with the two-electrode configuration, the as-synthesized catalyst on Ni foam (≈1.0 × 1.0 cm) was directly used as the cathode and anode. 1.0 M KOH solutions (pH 13.8) with or without different concentrations of HMF were used as the electrolytes. Linear sweep voltammetry (LSV) was conducted until the test results were stable at a scan rate of 5 mV s^{-1}.

The electrochemical surface area (ECSA) of the electrocatalyst was estimated from the electrochemical double-layer capacitance (C_{dl}), which was investigated *via* cyclic voltammetry (CV) cycles. The CV was performed in 1 M KOH with or without 5 mM HMF at various scan rates of 20, 40, 60, 80 and 100 mV s^{-1} in a non-faradaic potential window.

Electrochemical impedance spectroscopy (EIS) tests were measured over a frequency range from 10^{-2} to 106 Hz with an AC amplitude of 10 mV.

Product determination: the HMF, intermediates (HMFCA, FFCA, HMF, and DFF) and oxidation product (FDCA) were analyzed by high-performance liquid chromatography (HPLC, Agilent 1290 Infinity II) with an ultraviolet (UV)-visible detector (wavelength: 265 nm) and a Shim-pack GWS C18 (5 μm, 4.6 × 150 mm) column. The mobile phase was 75% ammonium formate together with 25% methanol. The flow rate was 0.2 mL min^{-1}. This mixture with a volume of 3 μL was then injected into the HPLC. The column temperature was maintained at 35 °C, and each separation lasts for 25 min. The conversion of HMF, selectivity and yield rate of FDCA were calculated according to eqn (2) and (3):

$$\text{HMF conversion}(\%) = [n(\text{HMF consumed})/n(\text{HMF initial})] \times 100 \quad (2)$$

$$\text{Product yield}(\%) = [n(\text{product})/n(\text{HMF initial})] \times 100 \quad (3)$$

where F represents the Faraday constant (96 485 C mol^{-1}), S is the electrode geometric area, and t is the electrolysis time (h).

Author contributions

Z. C., T. D. J. and S. L. conceived the experiments. Z. C., S. L., S. Liu, S. Li, J. L. and T. D. J. prepared the paper. X. Z. and L. S. were primarily responsible for the experiments and calculation. All the authors contributed to the data analysis.

Conflicts of interest

There are no conflicts to declare.

Acknowledgements

This work was supported by the National Natural Science Foundation of China (32171716, 31890774 (Z. C.)), the Natural Science Funding of Heilong Jiang province for Excellent Young Scholar (YQ2020C017 (Z. C.)), and The Open Research Fund of the School of Chemistry and Chemical Engineering, Henan Normal University (2020ZD01 (T. J.)).

References

1 X. Chen, S. Song, H. Li, G. Gozaydin and N. Yan, *Acc. Chem. Res.*, 2021, **54**, 1711–1722.
2 F. Cherubini, *Energy Convers. Manage.*, 2010, **51**, 1412–1421.
3 A. Corma, S. Iborra and A. Velty, *Chem. Rev.*, 2007, **107**, 2411–2502.
4 Y. Liao, S.-F. Koelewijn, G. Van den Bossche, J. Van Aelst, S. Van den Bosch, T. Renders, K. Navare, T. Nicolai, K. Van Aelst, M. Maesen, H. Matsushima, J. M. Thevelein, K. Van Acker, B. Lagrain, D. Verboekend and B. F. Sels, *Science*, 2020, **367**, 1385–1390.
5 Y. Jing, Y. Guo, Q. Xia, X. Liu and Y. Wang, *Chem*, 2019, **5**, 2520–2546.
6 J. Li, C. Chen, J. Y. Zhu, A. J. Ragauskas and L. Hu, *Acc. Mater. Res.*, 2021, **2**, 606–620.
7 A. Brandt, J. Grasvik, J. P. Hallett and T. Welton, *Green Chem.*, 2013, **15**, 550–583.
8 Y. Liu, N. Deak, Z. Wang, H. Yu, L. Hameleers, E. Jurak, P. J. Deuss and K. Barta, *Nat. Commun.*, 2021, **12**, 5424.
9 K. H. Kim, A. Eudes, K. Jeong, C. G. Yoo, C. S. Kim and A. Ragauskas, *Proc. Natl. Acad. Sci. U. S. A.*, 2019, **116**, 13816–13824.
10 Y. M. Questell-Santiago, M. V. Galkin, K. Barta and J. S. Luterbacher, *Nat. Rev. Chem.*, 2020, **4**, 311–330.
11 B. Zhang, T. Guo, Z. Li, F. E. Kuhn, M. Lei, Z. K. Zhao, J. Xiao, J. Zhang, D. Xu, T. Zhang and C. Li, *Nat. Commun.*, 2022, **13**, 3365.
12 E. L. Smith, A. P. Abbott and K. S. Ryder, *Chem. Rev.*, 2014, **114**, 11060–11082.
13 D. Yu, Z. Xue and T. Mu, *Cell Rep. Phys. Sci.*, 2022, **3**, 100809.
14 T. Renders, S. Van den Bosch, S. F. Koelewijn, W. Schutyser and B. F. Sels, *Energy Environ. Sci.*, 2017, **10**, 1551–1557.
15 L. Shuai, M. T. Amiri, Y. M. Questell-Santiago, F. Heroguel, Y. Li, H. Kim, R. Meilan, C. Chapple, J. Ralph and J. S. Luterbacher, *Science*, 2016, **354**, 329–333.
16 B. B. Hansen, S. Spittle, B. Chen, D. Poe, Y. Zhang, J. M. Klein, A. Horton, L. Adhikari, T. Zelovich and B. W. Doherty, *Chem. Rev.*, 2020, **121**, 1232–1285.
17 Y. Wan and J.-M. Lee, *ACS Catal.*, 2021, **11**, 2524–2560.
18 C. Li and Y. Na, *ChemPhotoChem*, 2021, **5**, 502–511.
19 O. Simoska, Z. Rhodes, S. Weliwatte, J. R. Cabrera-Pardo, E. M. Gaffney, K. Lim and S. D. Minteer, *ChemSusChem*, 2021, **14**, 1674–1686.
20 K. Ji, M. Xu, S. M. Xu, Y. Wang, R. Ge, X. Hu, X. Sun and H. Duan, *Angew. Chem., Int. Ed.*, 2022, **61**, e202209849.
21 Y. Lu, T. Liu, C. L. Dong, C. Yang, L. Zhou, Y. C. Huang, Y. Li, B. Zhou, Y. Zou and S. Wang, *Adv. Mater.*, 2022, **34**, 2107185.
22 T. Xia, W. Gong, Y. Chen, M. Duan, J. Ma, X. Cui, Y. Dai, C. Gao and Y. Xiong, *Angew. Chem., Int. Ed.*, 2022, **61**, e202204225.
23 J. N. Chang, Q. Li, Y. Yan, J. W. Shi, J. Zhou, M. Lu, M. Zhang, H. M. Ding, Y. Chen and S. L. Li, *Angew. Chem., Int. Ed.*, 2022, **61**, e202209289.
24 M. F. Kuehnel and E. Reisner, *Angew. Chem., Int. Ed.*, 2018, **57**, 3290–3296.
25 M. G. Davidson, S. Elgie, S. Parsons and T. J. Young, *Green Chem.*, 2021, **23**, 3154–3171.
26 J. Wang, X. Liu, Z. Jia, L. Sun and J. Zhu, *Eur. Polym. J.*, 2018, **109**, 379–390.
27 N. Zhang, Y. Zou, L. Tao, W. Chen, L. Zhou, Z. Liu, B. Zhou, G. Huang, H. Lin and S. Wang, *Angew. Chem., Int. Ed.*, 2019, **131**, 16042–16050.

28 J. Li, C. Hu, Y.-Y. Wang, X. Meng, S. Xiang, C. Bakker, K. Plaza, J. A. Ragauskas, Y. S. Dai and S. J. Yuan, *Matter*, 2022, **5**, 3513–3529.
29 Q. Xia, C. Chen, Y. Yao, J. Li, S. He, Y. Zhou, T. Li, X. Pan, Y. Yao and L. Hu, *Nat. Sustain.*, 2021, **4**, 627–635.
30 M. Zeng and X. Pan, *Catal. Rev.*, 2022, **64**, 445–490.
31 L. Chen, J. Dou, Q. Ma, N. Li, R. Wu, H. Bian, D. J. Yelle, T. Vuorinen, S. Fu, X. Pan and J. Zhu, *Sci. Adv.*, 2017, **3**, e1701735.
32 T. Zhang, *Science*, 2020, **367**, 1305–1306.
33 A. J. Ragauskas, G. T. Beckham, M. J. Biddy, R. Chandra, F. Chen, M. F. Davis, B. H. Davison, R. A. Dixon, P. Gilna and M. Keller, *Science*, 2014, **344**, 1246843.
34 X. Zhao, C. Huang, D. Xiao, P. Wang, X. Luo, W. Liu, S. Liu, J. Li, S. Li and Z. Chen, *ACS Appl. Mater. Interfaces*, 2021, **13**, 7600–7607.
35 J. Li, W. Liu, X. Qiu, X. Zhao, Z. Chen, M. Yan, Z. Fang, Z. Li, Z. Tu and J. Huang, *Green Chem.*, 2022, **24**, 823–836.
36 L. Zhou, X. Li, G. W. Ni, S. Zhu and J. Zhu, *Natl. Sci. Rev.*, 2019, **6**, 562–578.
37 J. Hong, C. Xu, B. Deng, Y. Gao, X. Zhu, X. Zhang and Y. Zhang, *Adv. Sci.*, 2022, **9**, 2103926.
38 H.-C. Ma, C.-C. Zhao, G.-J. Chen and Y.-B. Dong, *Nat. Commun.*, 2019, **10**, 3368.
39 S. Wang, D. Zhang, W. Wang, J. Zhong, K. Feng, Z. Wu, B. Du, J. He, Z. Li, L. He, W. Sun, D. Yang and G. A. Ozin, *Nat. Commun.*, 2022, **13**, 5305.
40 L.-Y. Chen, C.-W. Cheng and J.-Y. Liang, *Food Chem.*, 2015, **170**, 10–15.
41 L. Berstis, T. Elder, M. Crowley and G. T. Beckham, *ACS Sustain. Chem. Eng.*, 2016, **4**, 5327–5335.
42 G. Ulas, T. Lemmin, Y. Wu, G. T. Gassner and W. F. DeGrado, *Nat. Chem.*, 2016, **8**, 354–359.
43 N. Holten-Andersen, M. J. Harrington, H. Birkedal, B. P. Lee, P. B. Messersmith, K. Y. C. Lee and J. H. Waite, *Proc. Natl. Acad. Sci. U. S. A.*, 2011, **108**, 2651–2655.
44 S. Kim, A. U. Regitsky, J. Song, J. Ilavsky, G. H. McKinley and N. Holten-Andersen, *Nat. Commun.*, 2021, **12**, 1–10.
45 W. Huang, X. Xiao, C. Engelbrekt, M. Zhang, S. Li, J. Ulstrup, L. Ci, J. Feng, P. Si and Q. Chi, *Mater. Chem. Front.*, 2017, **1**, 1185–1193.
46 Y. Li, Y. Song, X. Zhang, T. Liu, T. Xu, H. Wang, D.-e. Jiang and R. Jin, *J. Am. Chem. Soc.*, 2022, **144**, 12381–12389.
47 Y. Wang, W. Zhu, W. Du, X. Liu, X. Zhang, H. Dong and W. Hu, *Angew. Chem., Int. Ed.*, 2018, **57**, 3963–3967.
48 J. Sun, E. Zhao, J. Liang, H. Li, S. Zhao, G. Wang, X. Gu and B. Z. Tang, *Adv. Mater.*, 2022, **34**, 2108048.
49 Y. Xie, Y. Qian, Z. Li, Z. Liang, W. Liu, D. Yang and X. Qiu, *ACS Sustain. Chem. Eng.*, 2021, **9**, 6479–6488.
50 A. Das and K. Mohanty, *Bioresour. Technol.*, 2023, **376**, 128884.
51 X. Liu, M. Park, M. G. Kim, S. Gupta, G. Wu and J. Cho, *Angew. Chem., Int. Ed.*, 2015, **54**, 9654–9658.
52 K. R. Vuyyuru and P. Strasser, *Catal. Today*, 2012, **195**, 144–154.
53 N. Niu, Z. Ma, F. He, S. Li, J. Li, S. Liu and P. Yang, *Langmuir*, 2017, **33**, 5786–5795.
54 X. Luo, C. Ma, Z. Chen, X. Zhang, N. Niu, J. Li, S. Liu and S. Li, *J. Mater. Chem. A*, 2019, **7**, 4002–4008.